Experimental Characterization of Thermal-Hydraulic Performance of a Microchannel Heat Exchanger for Waste Heat Recovery

James Yih[1] and Hailei Wang[2,*]

[1]School of Mechanical, Industrial & Manufacturing Engineering
Oregon State University, Corvallis, Oregon 97331
[2]Department of Mechanical and Aerospace Engineering
Utah State University, Logan, UT 84322

([*] Correspondence Author Email: hailei.wang@usu.edu)

Abstract

Given size and performance advantages, microchannel heat exchangers are becoming increasingly important for various energy recovery and conversion processes. In this study, detailed experimental measurements were conducted to characterize flow and heat transfer performance of a microchannel heat recovery unit (HRU) manufactured using standard photochemical etching and diffusion bonding processes. According to the global flow and temperature measurement, the HRU has delivered the predicted thermal performance under various oil and air flow rates. As expected, the heat transfer effectiveness varies between 88% and 98% for a given air and oil flow rates while it increases with air inlet temperature due to the improved thermal conductivity. However, significant flow mal distribution is identified among the air channels according to the in-depth flow distribution measurement using hot wire. The flow measurement also indicates visible misalignment of the air channels caused by the manufacturing processes. In addition, the excessive pressure drops occurred for both air and oil channels indicating reduced flow areas due to the photochemical etching process. The results of this experimental study can hopefully provide insights in improving designs of microchannel heat exchangers using the same manufacturing processes.

Keywords:
Microchannel heat exchanger, experimental characterization, thermal-hydraulic, flow distribution, organic Rankine cycle, waste heat recovery,

Nomenclature

Variables:

A *Cross-sectional area of an air channel*

D_h	*Hydraulic diameter*
$\dot{m}$	*Mass flow rate*
N	*Total number of air channels*
Re	*Reynolds number*
t	*Student's t distribution*
T	*Temperature*
u	*Error (uncertainty analysis)*
V	*Velocity*
ρ	*Density*
μ	*Viscosity*
ε	*Heat transfer effectiveness*

Subscripts:

Air	*the air side*
bias	*Bias error*
c	*the cold side of the fluid*
h	*the hot side of the fluid*
Oil	*the oil side*
pres	*Precision error*

Acronyms:

COP	*Coefficient of Performance*
HRU	*Heat recovery unit*
ORC	*Organic Rankine cycle*
TEG	*Thermoelectric generation*

1. Introduction

In the spirit of improving energy efficiency and mitigate climate change due to greenhouse gases emissions, waste heat recovery has been attracted significant research in recent years [1]–[4]. In general, there are three levels of waste heat that are loosely defined as: low grade, with temperatures less than 200 °C; medium grade, with temperatures greater than 200 °C and less than about 600 °C; and high grade, with temperatures greater than 600 °C [5]. Among various technologies for waste heat recovery, organic Rankine cycle (ORC) has been widely used for low-to-medium grade waste heat recovery systems and geothermal power plants [6], [7]. The technology has also been increasingly used for engine waste heat recovery [8]–[11]. A technical and economic analyses of using ORC for waste heat recovery from internal combustion engines is conducted [12]. For waste heat recovery of large stationary gaseous fuel internal combustion engines with rated power of 1 MW, both steam Rankine cycle and ORCs have been considered and shown respective pros and cons according to the technical and economic analyses [13]. For mobile applications with unsteady waste heat, dynamic simulation and control strategies need to be considered over various dynamic driving cycles [11], [14], [15]. Recently, an interesting waste heat recovery system using ORC is proposed for automotive engines in order to account for various dynamic driving situations [16]. It includes exhaust gas recirculation and thermal energy storage using metal blocks. According to the numerical simulation, the design significantly improves the operating stability and the overall efficiency of the ORC system. While improving system designs and performance, more and more studies have also been focused on design optimization of the ORC system for various objective functions [9], [17].

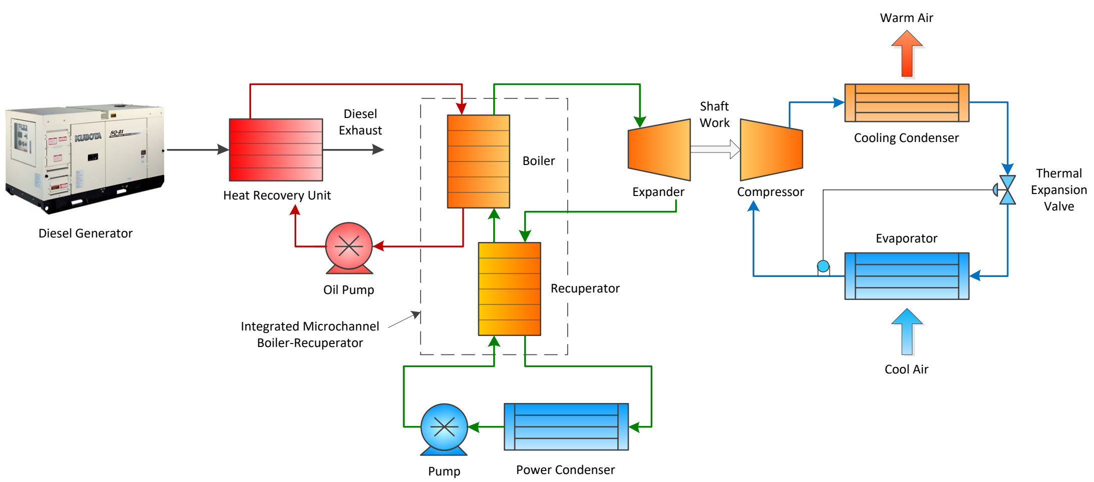

Figure 1. Waste heat-to-cooling system integrating an ORC with a vapor compression cycle

While most of the studies related to organic Rankine cycle for waste heat recovery have been focusing on converting the thermal energy to power, it is often desirable to convert waste heat to cooling directly for various cooling applications. An example of waste heat-to-cooling system utilizing ORC is shown in Figure 1. The system combines an ORC with a vapor-compression cycle to meet the cooling needs directly [18]. It is designed to produce cooling from the exhaust of a diesel engine. The waste heat recovery process starts at the diesel generator. Exhaust gases from the diesel generator pass through the Heat Recovery Unit and provide energy to the heat transfer oil. The oil is pumped through the boiler of the organic Rankine cycle, energizing the working fluid before it enters the expander. In this system, the expander is directly coupled to the compressor of a vapor-compression cycle to produce conditioned air.

As critical components, heat exchangers are crucial to the success of any waste heat recovery and energy conversion systems. With high surface area-to-volume ratio and increased heat transfer coefficients associated with short diffusion lengths, microchannel heat exchangers have become increasingly attractive for various energy conversion and management systems [19]–[22]. This often translates to considerably smaller package sizes with enhanced heat transfer [23]. In addition, the volume of working fluid necessary for operation is less than that of conventional heat exchangers, which potentially improves the safety for pressurized energy systems. With the ability to handle extremely high temperatures and pressures, they are considered as the top candidates for supercritical CO2 Brayton cycles [24]. In addition to straight channel designs [25], [26], various fin designs have been proposed to optimize thermal-hydraulic performance for supercritical CO2 recuperators, including zigzag [27], [28], S-shape [29], airfoil [30] and sinusoidal [24]. A recent review provides a good summary of recent experiment and numerical studies in understanding the flow and heat transfer characteristics associated with microchannel (printed circuit) heat exchangers [31].

While the studies provided valuable insights of flow and heat transfer within individual microchannel designs, significant questions still remain. For example, many studies have been focused on geometry design and numerical simulation for a single or only several channels. Thus, the results can be difficult to apply to real microchannel heat exchangers with hundreds or even thousands of microchannels due to potential flow maldistribution. According to a recent numerical and experimental study [32], flow maldistribution had very significant impact on heat transfer effectiveness of the device. Without uniform flow distribution in microchannel heat exchangers in a heat pump, a study shows up to 30% degradation of its cooling capacity is identified [33]. In addition, little work has been focused on in-depth, physical measurement of the actual flow and heat transfer performance of a sizeable, multi-channel and multi-layer microchannel heat exchanger. In this study, global and local characterizations of flow and heat transfer performance of a 10 kW-class microchannel prototype heat exchanger are performed. Specifically, it conducted a unique flow distribution study of a microchannel heat exchanger made by the standard photochemical etching and diffusion bonding processes. The work provided a useful measurement scheme of using hot wire and a 3-axis traverse system, and a post-measurement analysis tool for quantifying flow distribution among the microchannels. The results provide not only model validation, but also valuable insights in improving designs of high-performance microchannel heat exchanger.

2. Microchannel Heat Recovery Unit

The microchannel Heat Recovery Unit (HRU) is a two-pass, cross-counter flow microchannel heat exchanger. A schematic of this type of heat exchanger is shown in Figure 2. The Heat Recovery Unit was designed to operate as an intermediary between the diesel generator and the organic Rankine cycle. As such, there were physical and thermal considerations that influenced the design. Physically, the size of the HRU was limited by the space available within the chassis of the diesel generator. Thermally, the HRU had to work within the operating conditions of the diesel generator and organic Rankine cycle. Other factors, such as soot deposition and pressure drop, were also considered in the design. Based on the expected 5.3 kW cooling capacity of the vapor-compression cycle and an overall system COP of 0.5, the Heat Recovery Unit was designed to recover approximate10.6 kW of heat from the diesel engine. A thermal model was developed in MATLAB to optimize the heat transfer and geometry of the HRU to achieve this goal. Given the two-pass and cross-counter flow design, an iterative scheme was used to determine the fluid temperatures between the passes. The model first assumes the intermediate exhaust (air) temperature called midpass exhaust. The midpass oil temperature can be solved using ε-NTU method for the cold pass (section with blue arrows in Fig. 2). With hot exhaust (air) inlet temperature and oil inlet temperature (the calculated midpass oil temperature) known for the hot pass (section with red arrows in Fig. 2), a new midpass exhaust temperature is determined using the ε-NTU method, which becomes the updated input to the cold pass. Convergence is determined when the change in subsequent values of the intermediate exhaust temperature are less than 1E-3 °C. The solution algorithm of the thermal model is shown in Fig. 3.

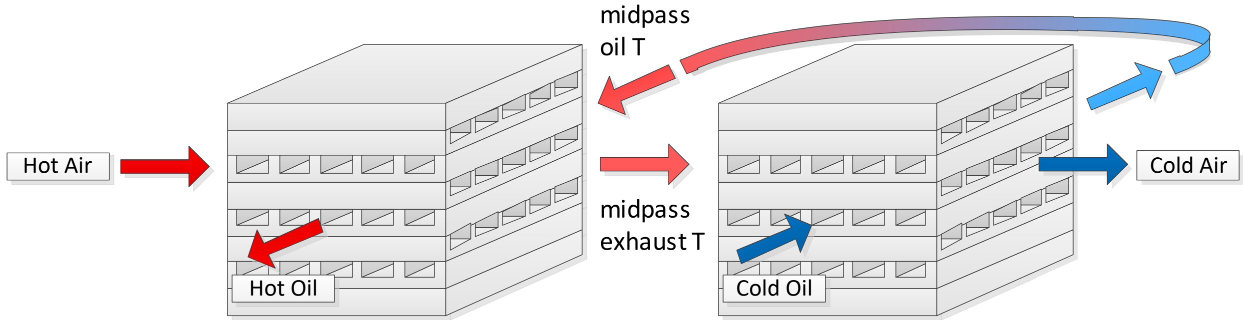

Figure 2. Two-pass, cross-counter flow plate-fin heat exchanger

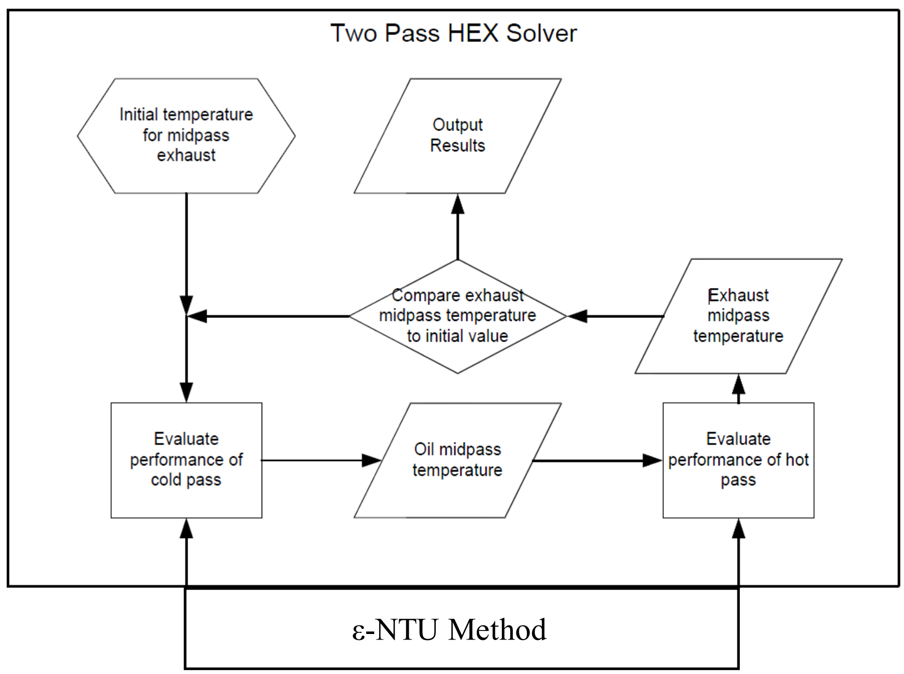

Figure 3. Solution algorithm for the heat exchanger thermal model

The Heat Recovery Unit is a diffusion brazed device that consists of a stack of alternating stainless-steel shims. The overall dimensions of the HRU model are 210 mm in length, 145 mm in width, and 85 mm in height. There are two different shim geometries in the Heat Recovery Unit. The first is the exhaust shim (also referred to as the air shim) and the second is the oil shim. Both shim types are designed with rectangular microchannels and are produced by photochemical etching. The exhaust channels are straight, with relatively wide cross-sectional area to reduce the back pressure on the engine and the potential of soot buildup from the diesel exhaust. Exhaust gases enter and leave through manifolds attached at the two ends of the heat exchanger. The oil shim contains two sections of channels that make up the two-pass flow arrangement. Flow distribution veins help guide the oil from the inlet port to the channels of the first pass. After the oil has passed through the first set of channels, it enters a plenum where it can mix with the oil from other layers before going through the second pass. The mixing plenum exists to increase heat transfer.

The design values of channel dimensions for both shims are shown in Table 1, while the design conditions and thermal model results for the HRU are shown in Table 2. Figure 4 shows the pictures of the fabricated HRU and the exhaust and oil shims. The objective of this study is to experimentally characterize the thermal-hydraulic performance of the microchannel HRU fabricated using a standard photochemical etching and diffusion brazing processes. The results will then be used to validate and refine heat transfer and flow models associated with microchannel heat exchangers.

Table 1. Channel dimensions and information of the shims

	Exhaust Shim	Oil Shim
Number of Channels	23	35 (per pass)
Channel Length (mm)	210	60
Channel Width (mm)	2.00	1.50
Channel Depth (mm)	0.80	0.15
Shim Thickness (mm)	0.99	0.30
Number of Shims in the Bonded Device	46	45

Table 2. Heat Recovery Unit design conditions and model results

Input Parameters		Model Results	
Air Inlet Temp (°C)	488	Air Outlet Temp (°C)	118
Oil Inlet Temp (°C)	100	Oil Outlet Temp (°C)	200
Air Flow (kg/s)	0.030	Duty (kW)	11.6
Oil Flow (kg/s)	0.046	Effectiveness	0.95
		Air Pressure Drop (kPa)	2.0
		Oil Pressure Drop (kPa)	22.0

Figure 4. (left) A photograph of the HRU showing air and oil inlets; (middle) Exhaust shim; (right) Oil shim

3. Experiment Setup and Analysis

The thermal testing facility had the capacity to test the thermal performance and measure velocity and temperature profiles of the Heat Recovery unit using hot air in place of diesel exhaust. A process and instrumentation diagram for the thermal testing facility is presented in Figure 5.

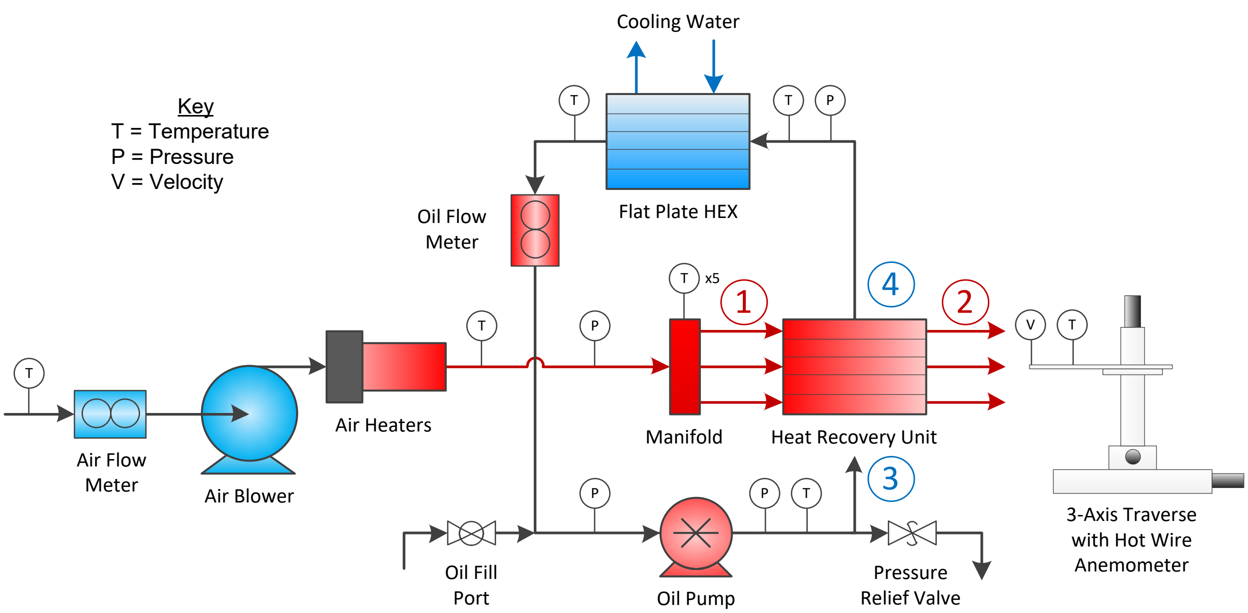

Figure 5. Heat Recovery Unit thermal test bench schematic

A regenerative blower intakes ambient air and passes it through two electrical air heaters. The hot air then enters a manifold where it is allowed to distribute before entering the exhaust channels of the Heat Recovery Unit (shown as stream 1 in Fig. 5). After the air exchanges heat with the oil in the HRU, it is exhausted into ambient air (shown as stream 2). A gear pump circulates oil through the HRU (stream 3 and 4) and into a flat plate heat exchanger. Cooling water runs through the flat plate heat exchanger to remove heat from the oil. A custom-built manifold was made for ducting the hot air into the Heat Recovery Unit. The manifold featured five holes for thermocouples to measure the air temperature distribution before it enters the heat exchanger. A pressure port was also included on the side to measure inlet pressure.

The instrumentation in the test bench included a hot wire anemometer, K-type thermocouples, 4-20 mA absolute pressure transducers, and turbine flow meters. A 3-axis linear traverse system was used to collect velocity and temperature measurements on the exhaust outlet of the Heat Recovery Unit. A single probe hot film anemometer (often referred to as a hot wire) was mounted to the LabVIEW controlled traverse system. The film had a sensing diameter of 25.4 µm and a length of 0.25 mm (recall that the exhaust channels were designed to 2 mm by 0.8 mm). A 1/16-in (~1.6 mm) diameter thermocouple was attached to the probe support. LabVIEW was used for the data acquisition and traverse control. A picture of the thermal testing facility is shown in Figure 6, where the HRU and traverse system are labelled to show the respective positions.

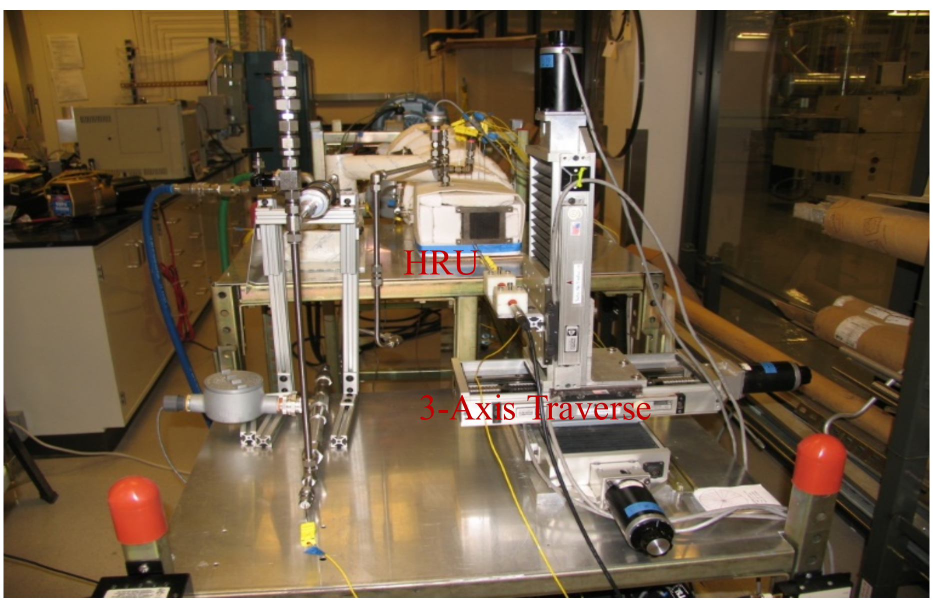

Figure 6. Thermal testing facility

The testing conditions used to evaluate the performance of the microchannel HRU are presented in Table 3. The nominal air inlet temperature was based on the average of the five manifold thermocouples.

The motivation behind the selected test values was to operate the HRU in a range that encompassed the design air flow rate, oil flow rate and air inlet temperature. For each thermal test case, steady state measurements were taken at 100 samples per second for three minutes. The thermocouple measuring the outlet air temperature from the HRU was located approximately in the center of the outlet plane and about 1 mm away from the face.

Table 3. Thermal test matrix

Nominal Flow Rates		Nominal Air Inlet Temperature (°C)				
		300	400	450		500
Air Flow (g/s)	Oil Flow (g/s)	Warm Oil (73 °C Inlet)		Cold Oil (53 °C Inlet)	Warm Oil (73 °C Inlet)	
20	40	x	x	x	x	x
	47	x	x	x	x	x
	55	x	x	x	x	x
23	40	x	x	x	x	x
	47	x	x	x	x	x
	55	x	x	x	x	x
27	40	x	x	x	Design	x
	47	x	x	x	x	x
	55	x	x	x	x	x

The traverse system was designed to move the hot wire and thermocouple sensors in a plane parallel to the exposed face of the microchannel HRU in order to characterize both velocity and temperature profiles of the air (exhaust) stream. Measurements were taken using a stop-and-go style of traversing. The hot wire and thermocouple were moved to a measurement position, and then data was acquired for a specified period of time before moving on to the next point. Two movement sequences were developed: a column-wise traverse and a row-wise traverse, as shown in Figure 7. These two sequence styles were mainly developed for program flexibility. The coordinate system used for the traverse measurements is drawn in Figure 8 (left). This coordinate system is only an indication of direction; it is not the origin of each scan. Each velocity scan has its own origin. The channels are numbered starting from the bottom left corner as shown in Figure 8 (right).

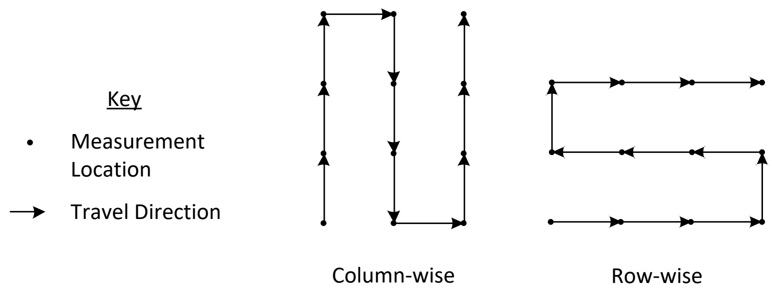

Figure 7. Scanning sequence styles

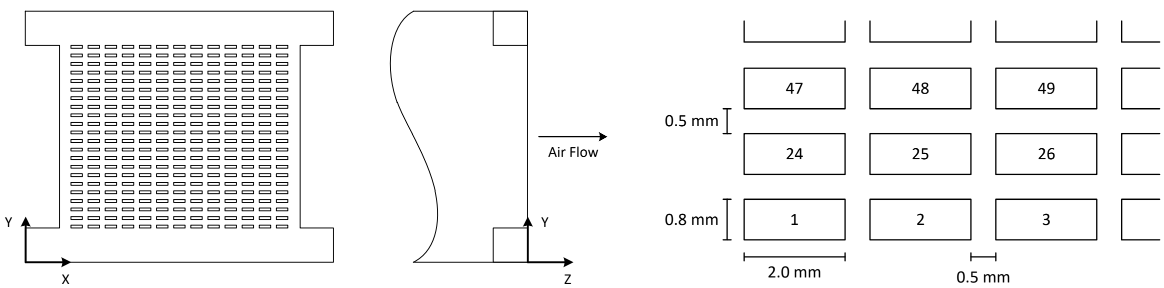

Figure 8. (left) Coordinate system for the traverse; (right) Air channel numbering and spacing

Velocity measurements were taken with unheated air at the design flow rate 27 g/s through the Heat Recovery Unit with no oil flow. In order to get adequate resolution of the channel velocities, measurements were taken in several regions instead of the full field because the acquisition time of a full field profile would have been impractical. To understand general trends in the air flow, the hot wire probe was traversed horizontally and vertically along the sides and middle channels of the HRU, as shown in Figure 9 (left). Window regions shown in Figure 9 (right) were also scanned to examine the flow structures near the channel outlets.

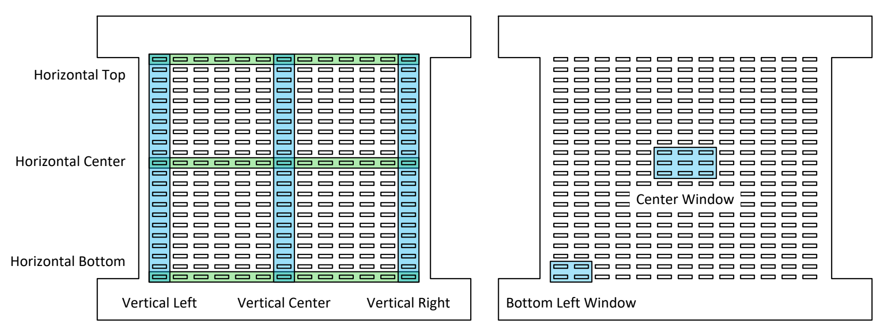

Figure 9. (left) Vertical and horizontal regions for hot wire measurements; (right) window regions

Vertical scans were executed using the column-wise movement scheme and the horizontal scans used the row-wise scheme. The window scans used the column-wise scheme. The scan resolution for each region is presented in Table 4. For all hot wire scan cases, at least 1,000 samples were collected over a period of one to two seconds for each measurement location. All velocity measurements were taken approximately 1 mm away from the face of the Heat Recovery Unit. The justification for this distance comes from measurements of the velocity in the z-direction for a center exhaust channel. As can be seen from the graph in Figure 10, the velocity was nearly constant within the range of 0.5 mm to 5 mm then it decreased as the probe moved away from the HRU face. This behavior resembles classical free jet theory.

Table 4. Scan resolutions

	Directional Resolution	
Scan Case	X (μm)	Y (μm)
Horizontal Top	200	100
Horizontal Center	200	100
Horizontal Bottom	200	100
Vertical Left	200	200
Vertical Center	200	200
Vertical Right	200	200
Center Window	100	100
Bottom Left Window	100	100
Full Temperature Field	1000	1000

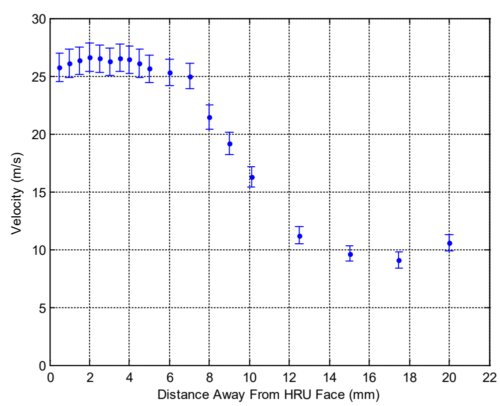

Figure 10. Air velocity as function of distance in the z-direction

A full field temperature profile was also captured for the nominal conditions of 27 g/s of air flow, 450 °C of air inlet temperature, 55 g/s of oil flow, and 60 °C of oil inlet temperature. The resolution for the thermal profile was 1 mm in both the x-direction and y-direction. Four hundred measurements were taken over three seconds for each location. The thermocouple was located approximately 2 mm away from the face of the HRU.

The thermal performance of the Heat Recovery Unit is characterized by the heat duty, heat transfer effectiveness, air pressure drop, and oil pressure drop. To evaluate the specific heat, the average of fluid inlet and outlet temperatures was used. For the air stream, the cold temperature was the average of the five manifold thermocouple readings. The hot temperature was taken from the thermocouple in the center of the air exit plane. Using air and oil temperatures, the effectiveness is defined as [34]:

$$\varepsilon = \frac{T_{Air,h} - T_{Air,c}}{T_{Air,h} - T_{Oil,c}} \tag{1}$$

The oil pressure drop across the microchannel HRU was taken as the difference between the two pressure measurements on the inlet and outlet of the oil line. The air pressure drop was measured by the single pressure transducer in the manifold (as outlet open to the atmosphere).

The theoretical air velocity out of the Heat Recovery Unit, assuming that the channels are the same size and uniform flow is

$$V = \frac{\dot{m}}{\rho\left(A \times N\right)} \tag{2}$$

where $\dot{m}$ is the air mass flow rate, ρ is the density of air, A is the cross-sectional area of an air channel, and N is the total number of air channels. The Reynolds number is defined as

$$\mathrm{Re} = \frac{\rho V D_h}{\mu} \tag{3}$$

where ρ is the density, V is the velocity, D_h is the hydraulic diameter, and μ is the dynamic viscosity. The Reynolds number can also be written in terms of the mass flow rate

$$\mathrm{Re}=\frac{\dot{m}D_h}{A\mu} \quad (4)$$

The velocity and temperature profiles were smoothed using a spatial averaging scheme. Each point is averaged with neighboring points up to two spaces away, including diagonals shown in Figure 11.

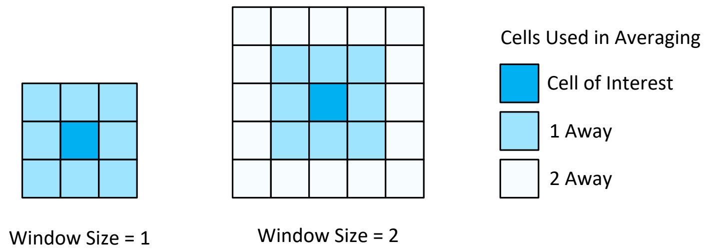

Figure 11. Averaging scheme for the velocity and temperature profiles

4. Uncertainty Analysis

The uncertainty of each measured variable was calculated using [35]:

$$u=\sqrt{u_{bias}^2+\left(t\times u_{pres}\right)^2} \quad (5)$$

where u_{bias} is the bias error, t is the Student's-t distribution factor, and u_{pres} is the precision error. The bias error of a measured variable consisted of the inherent limitations of the measuring instrument and the curve fit error of the calibration curve. Table 5 provides specific information and measurement accuracy of each instrument.

Table 5. Instrumentation specifications

Description	Manufacturer	Model Number	Range (Selected)	Accuracy
Hot Wire Anemometer	TSI	Model 1750 (System) 1260A-10A (Probe)	-	-
Turbine Flow Meter	OMEGA	FTB-938	8-130 acfm	1% Reading 0.25% Repeatability
Flow Meter Signal Conditioner	OMEGA	FLSC-61	75-375 Hz (350-1950 Hz) 1875-10000 Hz	0.3% FS Linearity
Turbine Flow Meter	OMEGA	FTB-901T	0.5-2.5 gpm	0.5% Reading 0.05% Repeatability
Flow Meter Signal Conditioner	OMEGA	FLSC-62A	(100-1000 Hz) 1 KHz-10 KHz	0.3% FS Linearity
Pressure Transducer	Cole-Parmer	68075-18	0-100 psig	0.25% FS
Pressure Transducer	Cole-Parmer	68075-16	0-50 psig	0.25% FS
Pressure Transducer	OMEGA	PX209-030A5V	0-30 psia	0.25% FS
Thermocouple	OMEGA	KMQSS-062U-6 KMQSS-062E-6	-200 to 1250 °C	Greater of 2.2 °C or 0.75%

The Student's-t statistic for a 95% confidence interval was taken as 1.96 for all measurements because the number of measurement samples was large (> 60), and hence a large degree of freedom. The precision error was taken as the standard deviation of the measurements, usually multiplied by the slope of the calibration curve if necessary. Table 6 lists the average relative uncertainty for the measured variables.

Propagation of the uncertainties to a derived quantity, such as the fluid energies and the effectiveness, was calculated using the root-sum-square method [35]. The average relative uncertainties of the calculated quantities are summarized in Table 7. Specific uncertainties of measured and calculated quantities are presented as error bars in the results sections.

$$u_y = \pm\sqrt{\sum_i \left(\left.\frac{\partial y}{\partial x_i}\right|_{x=\bar{x}} \times u_{x_i} \right)^2} \tag{6}$$

Table 6. Average relative uncertainty of measured quantities

Measurement		Average Relative Uncertainty
Flow Rate	Air Volumetric Flow Rate (m^3/s)	2%
	Oil Volumetric Flow Rate (m^3/s)	2%
Pressures	Air Manifold Pressure (kPa)	4%
	Oil Pump Pressure In (kPa)	1%
	Oil Pump Pressure Out (kPa)	1%
	HRU Oil Pressure In (kPa)	1%
	HRU Oil Pressure Out (kPa)	1%
Temperatures	Manifold Temperatures (°C)	1%
	HRU Air Outlet Temperature (°C)	3%
	Air After Heaters Temperature (°C)	1%
	Ambient Air Inlet Temperature (°C)	9%
	HRU Oil Inlet Temperature (°C)	4%
	HRU Oil Outlet Temperature (°C)	1%
	After Flat Plate HEX Temperature (°C)	4%

Table 7. Average relative uncertainty of calculated quantities

Calculated Quantity		Average Relative Uncertainty
Fluid Properties	Average Air Temperature [Manifold & Outlet] (°C)	1%
	Average Air Specific Heat (kJ/kg-K)	0.04%
	Air Inlet Density (kg/m^3)	1%
	Average Oil Temperature [HRU Inlet & Outlet] (°C)	1%
	Average Oil Specific Heat (kJ/kg-K)	1%
	Average Oil Density (kg/m^3)	0.2%
Mass Flow	Air Mass Flow Rate (g/s)	2%
	Oil Mass Flow Rate (g/s)	2%
Thermal Performance	Average Manifold Temperature (°C)	0.2%
	Air Energy (kW)	2%
	Oil Energy (kW)	5%
	Effectiveness (%)	1%
	Air Pressure Drop (kPa)	4%
	Oil Pressure Drop (kPa)	2%

As shown, a measurement that had a high relative uncertainty was the ambient air inlet temperature. This measurement was located at the inlet of the air blower and was used to calculate the air density near the flow meter. This seemingly high uncertainty in the measured temperature did not significantly affect the calculations because the density of air is not very sensitive to small changes in temperature. The primary contributor to the uncertainty of the oil energy was the oil mass flow rate.

The positional accuracy and repeatability of the traverse stages was 23 μm and 5 μm, respectively, over the full travel range. Each stage had a linear encoder that was used in conjunction with the motor driver to position the stage precisely. The encoders had a resolution of 5 μm. Using the root-sum-square method from Figliola and Beasley [35], the uncertainty of travel was calculated as 25 μm. On average, the uncertainty of the velocity measurements was 2 m/s. The velocity uncertainty was dominated by the level of fluctuations in the readings (standard deviation). Where there was more flow and turbulence, the fluctuations were larger.

5. Results and Discussions

5.1 Thermal-hydraulic Performance Tests

For all thermal tests, the manifold thermocouples indicated a uniform air temperature distribution into the Heat Recovery Unit. Graphical results of the duty, effectiveness, air pressure drop, and oil pressure drop are presented in the following subsections. Additionally, comparisons of performance between cases with a warm oil inlet temperature (73 °C average) and a cold oil inlet temperature (53 °C average) are shown and discussed.

The heat duty (overall heat transfer rate) is presented as the oil energy, reflecting the energy change per unit mass flow per unit time. Figures 12-14 display the heat duty for each constant oil flow rate. These tests were conducted with an oil inlet temperature near 73 °C, which is closest to the design point of the microchannel HRU. For a constant oil mass flow rate, higher air inlet temperature increases the amount of energy picked up by the oil. Similarly, as the air mass flow rate increases, so does the oil energy. Increasing the air inlet temperature and the air mass flow rate effectively increases the available energy for exchange. Meanwhile the increased heat duty is also attributed to improved thermal conductivity for air at higher temperature and improved average heat transfer coefficient for air at higher mass flow rates. For 40 g/s oil mass flow rate (Figure 12), the experimental results are consistently higher than the model predictions, even when considering the uncertainty. However, for the cases of 47 g/s and 55 g/s of oil flow, the experimental heat transfers match the predicted heat transfer to within the estimated uncertainty. An investigation later revealed that the calibration of the oil flow meter using the catch and weigh method may have over-estimate the oil flow rate at lower flow rates.

Overall, the model predicted the heat transfer of the microchannel HRU very well. For the air energy, the model agreed with the experimental values almost exactly (less than 1% difference). Even though the geometric characterization indicates that the flow areas of the microchannels were smaller than the design, it did not significantly degrade the heat transfer performance of the Heat Recovery Unit. This is likely because the hydraulic diameters did not significantly deviate from the design.

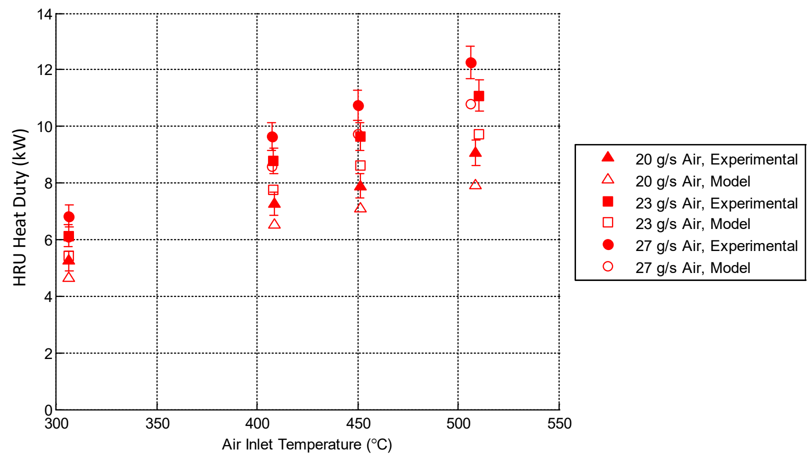

Figure 12. Heat Duty for 40 g/s warm oil flow

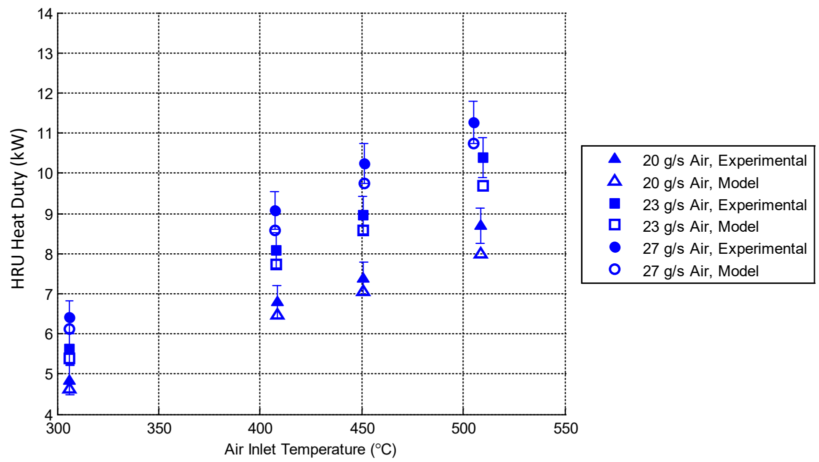

Figure 13. Heat Duty for 47 g/s warm oil flow

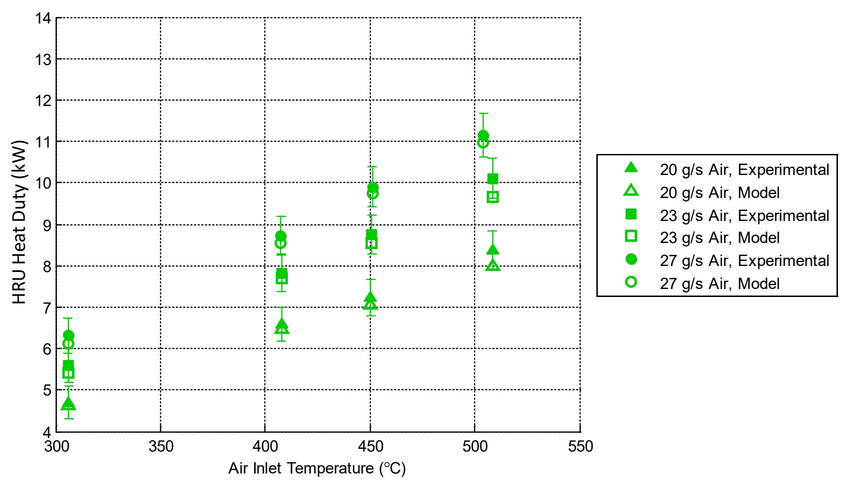

Figure 14. Heat Duty for 55 g/s warm oil flow

The heat transfer effectiveness for the three oil flow rates are shown in Figures 15-17. These plots also correspond to the tests with the warm oil inlet temperature. As shown, the effectiveness increased slightly as the inlet air temperature increased. Unlike the heat duty, the effectiveness decreased when the air mass flow rate increased. The effectiveness seems to be insensitive to oil flow rate for these conditions. Nearly all of the experimental data matches the model predictions within the uncertainty. For those that do not fall within the uncertainty, the difference is minimal. The very slight discrepancy in the effectiveness for a few cases could be due to the air outlet temperature measurement. The air outlet temperature was only measured at a single location for the thermal tests. The thermocouple was placed at the center of the air exhaust plane, 1 mm away from the face of the HRU. Since it is unlikely that the flow was entirely uniform, as the model presumes, the location of the air outlet temperature measurement may influence the resulting effectiveness. In general, the results of the effectiveness confirm that the microchannel HRU performed as the model predicted.

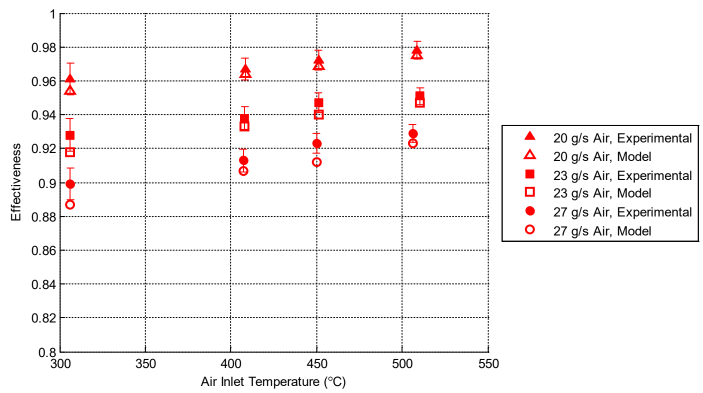

Figure 15. Effectiveness for 40 g/s warm oil flow

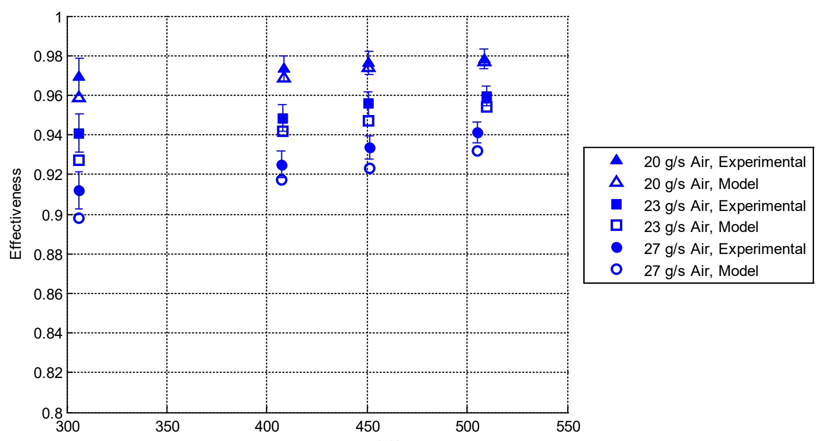

Figure 16. Effectiveness for 47 g/s warm oil flow

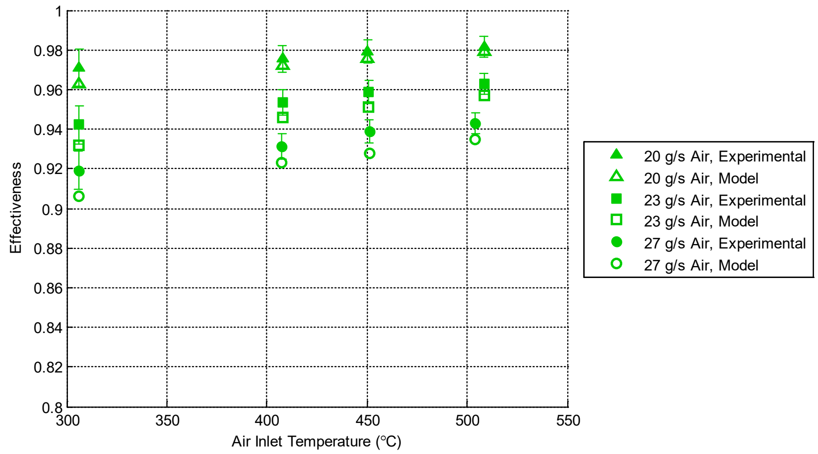

Figure 17. Effectiveness for 55 g/s warm oil flow

The air pressure drop is plotted versus the air mass flow rate in Figure 18. The plot shows that the air pressure drop was significantly more than what the model predicted for all the test cases. The general trend of increasing pressure drop as flow rate increases is displayed by both the experimental data and the model prediction. The pressure drop also increases for an increase in the air temperature, as expected, as the viscosity of air increases with the temperature. The factor that likely contributes the most to the discrepancy of the pressure drop is the channel cross-sectional area. Since the actual air channels are smaller than the design, significantly larger pressure drop is expected.

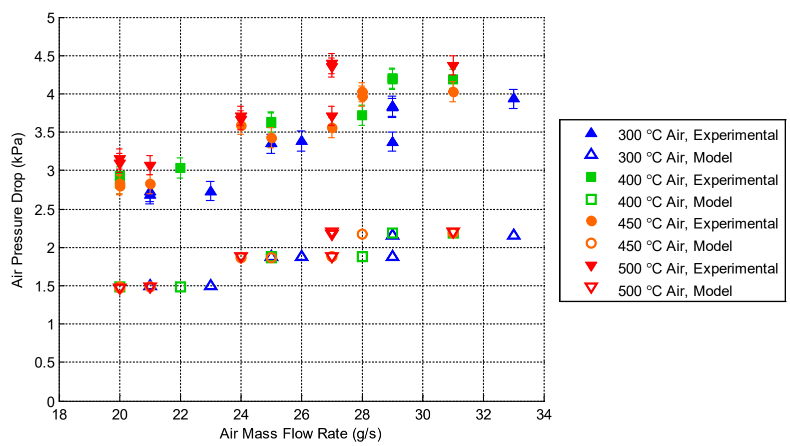

Figure 18. Air pressure drop as function of mass flow rate

The oil pressure drop is plotted versus oil inlet temperature in Figure 19. The experimental data shows that the oil pressure drop tends to decrease as the temperature increases. This is because the viscosity of the oil is sensitive to temperature. As the oil inlet temperature increases, its viscosity decreases resulting in lower pressure drops. As the oil mass flow rate increases, the pressure drop also increases. However, the magnitude of the experimental data is significantly different from the model predictions by consistently more than a factor of two. The same explanations discussed in the previous section for the inconsistency between the experimental and model results of the air pressure drop are also valid for the oil pressure drop. The smaller cross-sectional area and shape of the oil channels likely caused the conflict between the measured data and the model prediction. In addition, the model does not account for any of the header and plenum features within the oil passages. For example, there are significant constrictions at the inlet and outlet of the oil ports. Also, the plenum area between the two passes could have contributed to significant oil pressure drops.

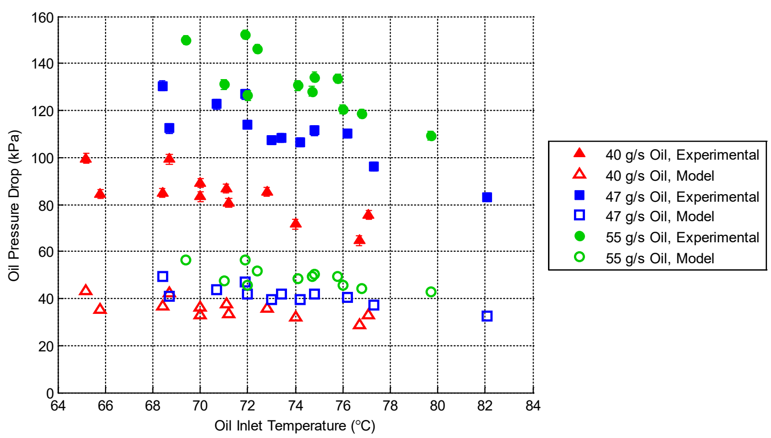

Figure 19. Oil pressure drop as function of inlet temperature

5.2 Hot Wire Flow Distribution Tests

All the velocity measurements were taken with unheated air (25 °C inlet) at an air mass flow rate of 27 g/s. Several plots of the horizontal and vertical velocity scans are presented in this section. Figure 20 shows 3-D plots of each scan (noted the x and y directions are in different scales). The contour plots of the horizontal and vertical scans are shown in Figures 21 and 22. Velocity profiles of individual channels are distinguishable in the figures. Each figure shows that the velocity magnitudes were fairly uniform within the scan. Out of all six scans, the horizontal center scan showed more consistent and higher air velocities (approaching 20 m/s). A peculiarity of the horizontal and vertical scans is that the peak velocities do not match where the scans should intersect. The reason why the scans do not match is likely due to the resolution of the traverses. The vertical scans were taken with a resolution of 200 µm in the x-direction and 200 µm in the y-direction, whereas the horizontal scans were taken with a resolution of 200 µm in the x-direction and 100 µm in the y-direction. The horizontal scans were deemed more accurate at characterizing the flow than the vertical scans because the resolution was finer.

From Figures 21 and 22, it can be seen that there are some channels missing in the horizontal bottom scan. This could be due to some blockage in the channels (potentially during the diffusion brazing process). Similarly, the vertical right scan is missing a channel at the bottom. In addition, the horizontal top velocity scan and all vertical scans have depicted the poor channel alignment due to fabrication. According to the measurement, more flow is reached to the center channels than the top and bottom channels. Presumably, the diffusion bonding process may have also deformed some of the top and bottom channels and exacerbated the mis-alignment.

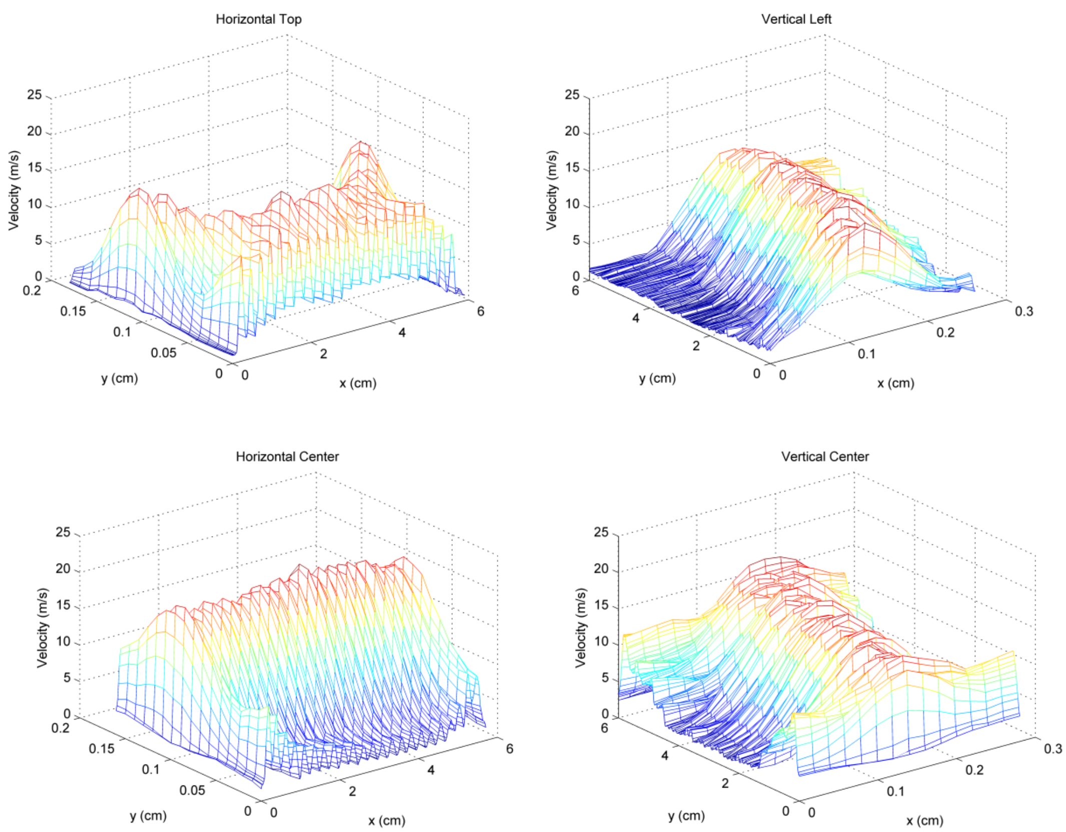

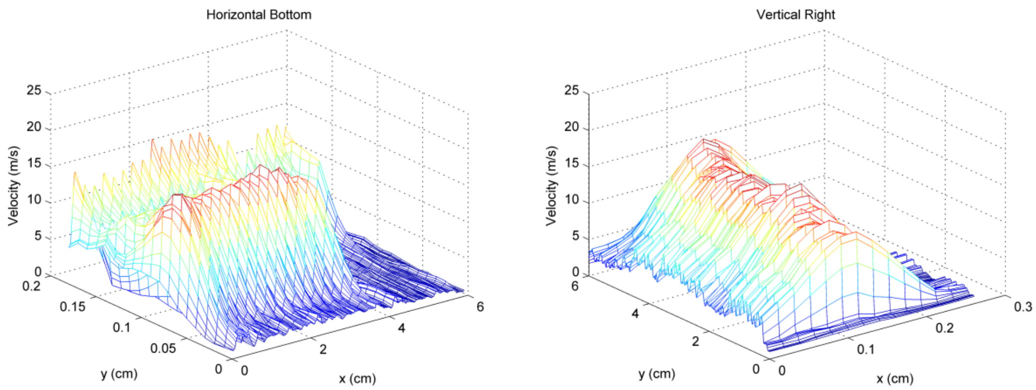

Figure 20. 3-D plots of horizontal and vertical velocity scans

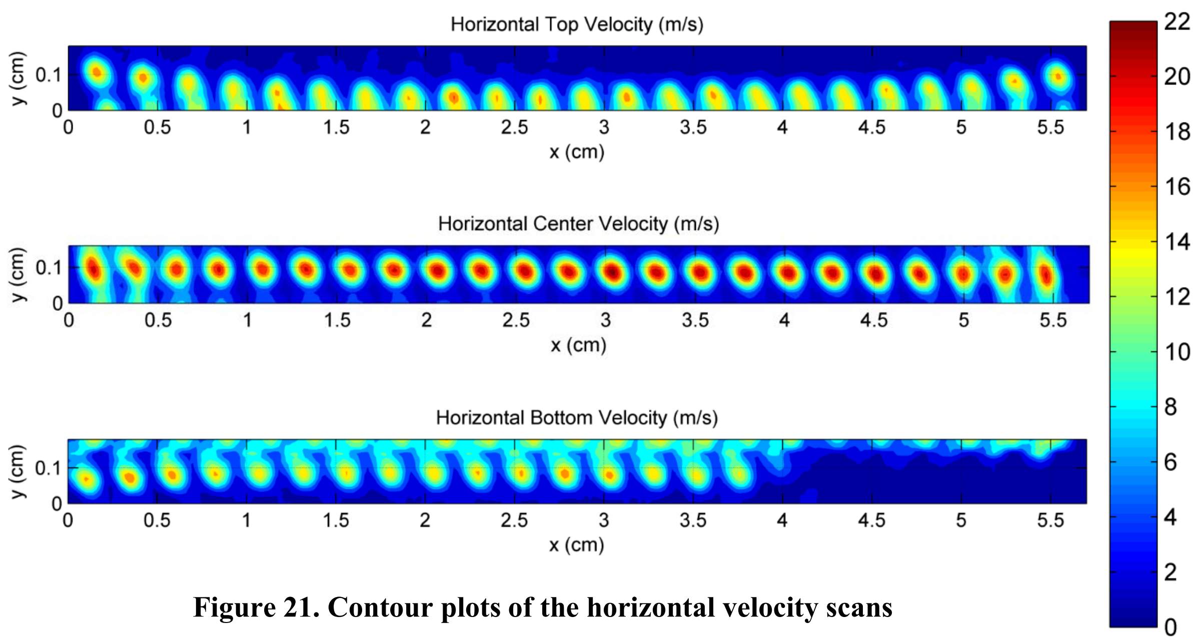

Figure 21. Contour plots of the horizontal velocity scans

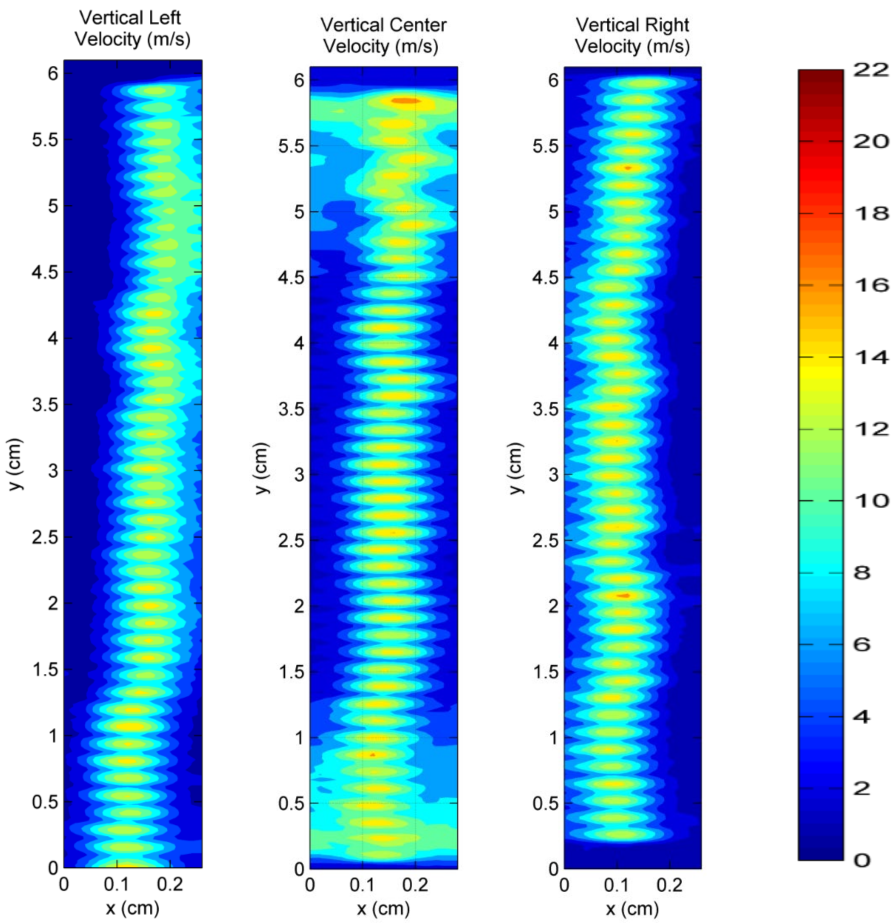

Figure 22. Contour plots of the vertical velocity scan

Figures 23 and 24 display the results of the center window scan and the bottom left window scan. The window scans were taken with the highest resolution of all the traversing schemes at 100 µm in both the x and y directions. The largest magnitudes collected for the window scans agree with the results of the horizontal scans, which confirms that the resolution was an issue. For the nine microchannels captured in the center window scan, their velocity profiles appear to be very uniform in the center region. Similarly, velocities appear fairly uniform in the four microchannels of the bottom left window. On the global scale, however, the flow distribution is not very uniform across all air channels, which is also identified in a full-field maximum velocity interpolation study.

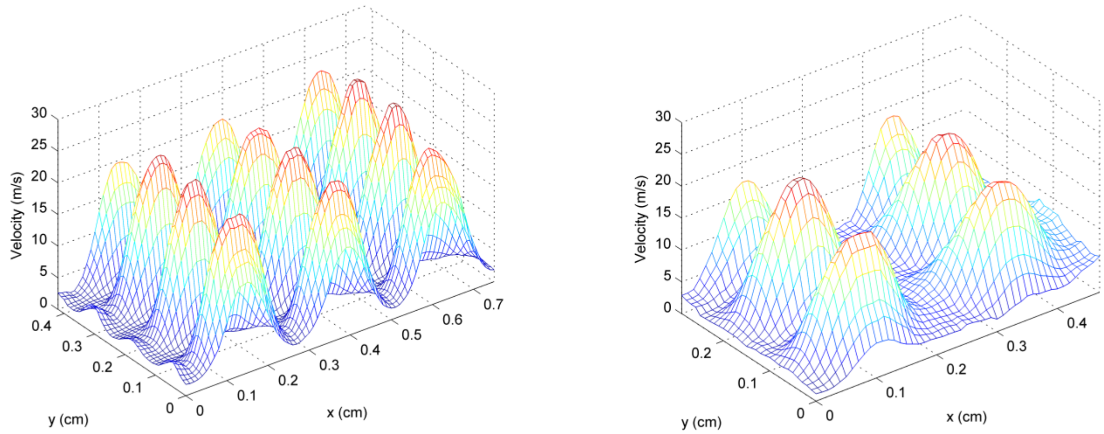

Figure 23. 3-D velocity plot of the center window (left); the bottom left window (right)

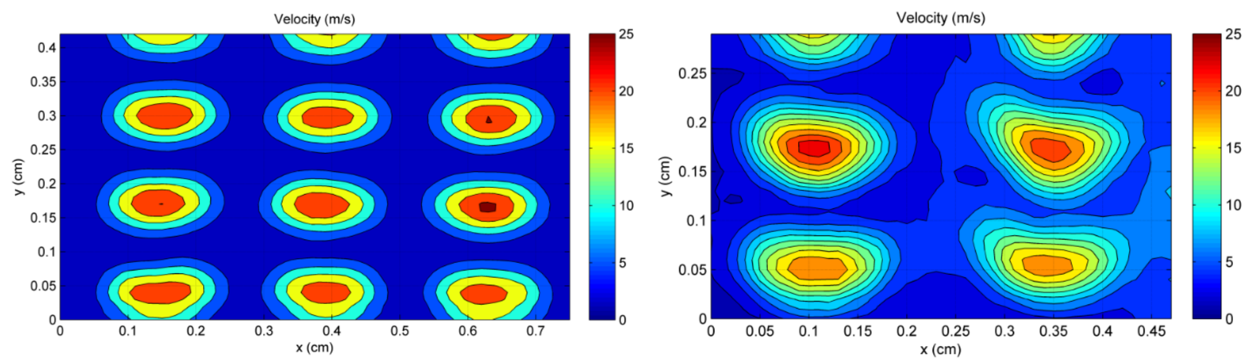

Figure 24. Velocity contour plot of the center window (left); the bottom left window (right)

5.3 Full Field Temperature Test

A full field temperature profile was measured for one case of thermal loading. The testing conditions are tabulated in Table 8. Measurements were taken at a resolution of 1 mm in both the x and y directions, approximately 2 mm away from the HRU face. The temperature profile's non-uniform shape (as shown in Figure 25) is indicative of the heat transfer and flow of the Heat Recovery Unit. The air along the outer regions of the channel array was cooled more than the air in the center, resulting in lower temperatures on the sides and higher temperatures in the middle. The left and right sides of the profile are not mirrored. On the left side, the temperature contours show that there was slightly more cooling than on the right. This can be attributed to the geometry of the HRU. Recall that, in this view, the header ports for the oil are located on the left side. The inlet oil starts cold on the left side then warms up as it travels to the right, picking up heat from the air stream. Consequently, the exhaust air was cooler on the left and warmer on the right because more heat transfer occurred on the left.

Table 8. Test conditions for the full field temperature profile

Controlled Parameters		Heat Exchanger Performance	
Air Mass Flow Rate (g/s)	27	Average Outlet Air Temperature (°C)	72
Inlet Air Temperature (°C)	451		
Oil Mass Flow Rate (g/s)	56	Outlet Oil Temperature (°C)	155
Inlet Oil Temperature (°C)	62	Heat Transfer [Based on Oil Energy] (kW)	11.8
		Effectiveness	0.97
		Air Pressure Drop (kPa)	3
		Oil Pressure Drop (kPa)	200

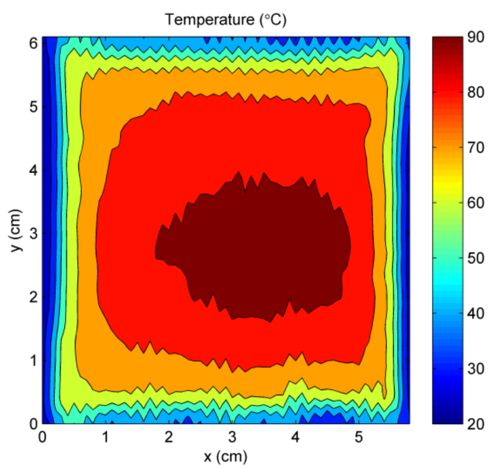

Figure 25. Full field temperature profile for conditions close to the design

6. Conclusions

The study performed a comprehensive experimental characterization on the flow and heat transfer performance of a nominal (design value) 10.6 kW microchannel heat recovery unit manufactured using standard photochemical etching and diffusion bonding processes. In addition to global performance assessment in terms of heat transfer effectiveness and pressure drops, local flow and temperature measurements were performed to quantify flow distribution. Based on the results, the following conclusions are drawn from the study:

1) The microchannel HRU upheld the predicted thermal performance under various oil and air flow rates. The heat transfer effectiveness varied between 88% and 98%.
2) For a given oil flow rate, the overall heat transfer (heat duty) increased with air flow while the effectiveness decreased with air flow. The effectiveness increased with air inlet temperature as the result of its higher thermal conductivity.
3) Significant flow mal distribution was identified among the air channels according to the flow measurement using hot wire. The flow measurement also showed visible misalignment of the air channels and even flow blockage caused by the manufacturing processes.
4) Significantly higher pressure drops were encountered for both air and oil channels, which can be largely attributed to reduced flow areas due to the photochemical etching process.
5) The findings shed some lights in improving designs of microchannel heat exchangers, which should consider the capabilities and limitations of the manufacturing processes.

7. Acknowledgement

The authors would like to thank the financial support provided by US Army CERDEC Tactical Energy System Program.

8. References

[1] A. Mahmoudi, M. Fazli, and M. R. Morad, “A recent review of waste heat recovery by Organic Rankine Cycle,” *Appl. Therm. Eng.*, vol. 143, pp. 660–675, 2018.
[2] B. Xu, D. Rathod, A. Yebi, Z. Filipi, S. Onori, and M. Hoffman, “A comprehensive review of organic rankine cycle waste heat recovery systems in heavy-duty diesel engine applications,” *Renew. Sustain. Energy Rev.*, vol. 107, pp. 145–170, 2019.
[3] V. Chintala, S. Kumar, and J. K. Pandey, “A technical review on waste heat recovery from compression ignition engines using organic Rankine cycle,” *Renew. Sustain. Energy Rev.*, vol. 81, pp. 493–509, 2018.
[4] L. Shi, G. Shu, H. Tian, and S. Deng, “A review of modified Organic Rankine cycles (ORCs) for internal combustion engine waste heat recovery (ICE-WHR),” *Renew. Sustain. Energy Rev.*, vol. 92, pp. 95–110, 2018.
[5] Industrial Technologies Program, “Waste Heat Recovery: Technology and Opportunitites in U.S. Industry.” US Department of Energy, 2008.
[6] N. Kazemi and F. Samadi, “Thermodynamic, economic and thermo-economic optimization of a new proposed organic Rankine cycle for energy production from geothermal resources,” *Energy Convers. Manag.*, vol. 121, pp. 391–401, 2016.

[7] F. Moloney, E. Almatrafi, and D. Y. Goswami, “Working fluid parametric analysis for regenerative supercritical organic Rankine cycles for medium geothermal reservoir temperatures,” *Energy Procedia*, vol. 129, pp. 599–606, 2017.

[8] A. T. Hoang, “Waste heat recovery from diesel engines based on Organic Rankine Cycle,” *Appl. Energy*, vol. 231, pp. 138–166, 2018.

[9] Y. Zhu, W. Li, G. Sun, and H. Li, “Thermo-economic analysis based on objective functions of an organic Rankine cycle for waste heat recovery from marine diesel engine,” *Energy*, vol. 158, pp. 343–356, 2018.

[10] Z. M. Nawi, S. K. Kamarudin, S. R. S. Abdullah, and S. S. Lam, “The potential of exhaust waste heat recovery (WHR) from marine diesel engines via organic rankine cycle,” *Energy*, vol. 166, pp. 17–31, 2019.

[11] W. R. Huster, Y. Vaupel, A. Mhamdi, and A. Mitsos, “Validated dynamic model of an organic Rankine cycle (ORC) for waste heat recovery in a diesel truck,” *Energy*, vol. 151, pp. 647–661, 2018.

[12] R. de O. Neto, C. A. R. Sotomonte, C. J. R. Coronado, and M. A. R. Nascimento, “Technical and economic analyses of waste heat energy recovery from internal combustion engines by the Organic Rankine Cycle,” *Energy Convers. Manag.*, vol. 129, pp. 168–179, 2016.

[13] G. Shu, X. Wang, and H. Tian, “Theoretical analysis and comparison of rankine cycle and different organic rankine cycles as waste heat recovery system for a large gaseous fuel internal combustion engine,” *Appl. Therm. Eng.*, vol. 108, pp. 525–537, 2016.

[14] V. Grelet, T. Reiche, V. Lemort, M. Nadri, and P. Dufour, “Transient performance evaluation of waste heat recovery rankine cycle based system for heavy duty trucks,” *Appl. Energy*, vol. 165, pp. 878–892, 2016.

[15] S. Kim, K. Choi, K. Lee, and K. Kim, “Evaluation of automotive waste heat recovery for various driving modes,” *Energy*, vol. 106, pp. 579–589, 2016.

[16] R. Shi, T. He, J. Peng, Y. Zhang, and W. Zhuge, “System design and control for waste heat recovery of automotive engines based on Organic Rankine Cycle,” *Energy*, vol. 102, pp. 276–286, 2016.

[17] M. Imran, F. Haglind, V. Lemort, and A. Meroni, “Optimization of organic rankine cycle power systems for waste heat recovery on heavy-duty vehicles considering the performance, cost, mass and volume of the system,” *Energy*, vol. 180, pp. 229–241, 2019.

[18] H. Wang *et al.*, “Performance of a combined organic Rankine cycle and vapor compression cycle for heat activated cooling,” *Energy*, vol. 36, no. 1, pp. 447–458, 2011.

[19] S. Baek, J.-H. Kim, S. Jeong, and J. Jung, “Development of highly effective cryogenic printed circuit heat exchanger (PCHE) with low axial conduction,” *Cryogenics*, vol. 52, no. 7, pp. 366–374, Jul. 2012.

[20] V. R. Saranam and B. K. Paul, “Feasibility of Using Diffusion Bonding for Producing Hybrid Printed Circuit Heat Exchangers for Nuclear Energy Applications,” *Procedia Manuf.*, vol. 26, pp. 560–569, Jan. 2018.

[21] D. A. Kromer, A. J. Huning, and S. Garimella, “I2S-LWR microchannel heat exchanger design and experimental validation,” *Ann. Nucl. Energy*, Sep. 2017.

[22] L. Chai and S. A. Tassou, “Numerical study of the thermohydraulic performance of printed circuit heat exchangers for supercritical CO2 Brayton cycle applications,” *Energy Procedia*, vol. 161, pp. 480–488, Mar. 2019.

[23] M. Pan *et al.*, “Experimental investigation of the heat transfer performance of microchannel heat exchangers with fan-shaped cavities,” *Int. J. Heat Mass Transf.*, vol. 134, pp. 1199–1208, May 2019.

[24] M. Saeed and M.-H. Kim, “Thermal-hydraulic analysis of sinusoidal fin-based printed circuit heat exchangers for supercritical CO2 Brayton cycle,” *Energy Convers. Manag.*, vol. 193, pp. 124–139, Aug. 2019.

[25] Z. Zhao, X. Zhang, K. Zhao, P. Jiang, and Y. Chen, "Numerical investigation on heat transfer and flow characteristics of supercritical nitrogen in a straight channel of printed circuit heat exchanger," *Appl. Therm. Eng.*, vol. 126, pp. 717–729, Nov. 2017.

[26] T. Dang, J. Teng, and J. Chu, "A study on the simulation and experiment of a microchannel counter-flow heat exchanger," *Appl. Therm. Eng.*, vol. 30, no. 14, pp. 2163–2172, Oct. 2010.

[27] S.-J. Yoon, J. O'Brien, M. Chen, P. Sabharwall, and X. Sun, "Development and validation of Nusselt number and friction factor correlations for laminar flow in semi-circular zigzag channel of printed circuit heat exchanger," *Appl. Therm. Eng.*, vol. 123, pp. 1327–1344, Aug. 2017.

[28] T. Ma, U. Pasquier, Y. Chen, and Q. Wang, "Numerical study on thermal-hydraulic performance of a two-sided etched zigzag-type high-temperature printed circuit heat exchanger," *Energy Procedia*, vol. 142, pp. 3950–3955, Dec. 2017.

[29] T. L. Ngo, Y. Kato, K. Nikitin, and T. Ishizuka, "Heat transfer and pressure drop correlations of microchannel heat exchangers with S-shaped and zigzag fins for carbon dioxide cycles," *Exp. Therm. Fluid Sci.*, vol. 32, no. 2, pp. 560–570, Nov. 2007.

[30] X. Cui, J. Guo, X. Huai, K. Cheng, H. Zhang, and M. Xiang, "Numerical study on novel airfoil fins for printed circuit heat exchanger using supercritical CO2," *Int. J. Heat Mass Transf.*, vol. 121, pp. 354–366, Jun. 2018.

[31] C. Huang, W. Cai, Y. Wang, Y. Liu, Q. Li, and B. Li, "Review on the characteristics of flow and heat transfer in printed circuit heat exchangers," *Appl. Therm. Eng.*, vol. 153, pp. 190–205, May 2019.

[32] S. Baek, C. Lee, and S. Jeong, "Effect of flow maldistribution and axial conduction on compact microchannel heat exchanger," *Cryogenics*, vol. 60, pp. 49–61, Mar. 2014.

[33] Y. Zou, H. Tuo, and P. S. Hrnjak, "Modeling refrigerant maldistribution in microchannel heat exchangers with vertical headers based on experimentally developed distribution results," *Appl. Therm. Eng.*, vol. 64, no. 1, pp. 172–181, Mar. 2014.

[34] F. P. Incropera, and D. P. DeWitt, *Fundamentals of Heat and Mass Transfer*, 4th ed. Wiley.

[35] R. Figliola and D. Beasley, *Theory and Design for Mechanical Measurements.*, 2nd ed. Wiley, 1995.